First Results from HaloSat - A CubeSat to Study the Hot Galactic Halo

P. Kaaret, A. Zajczyk, D. LaRocca, D.L. Kirchner, W. T. Robison, J. Bluem, W. Fuelberth, H. Gulick, J. Haworth,
R. McCurdy, D. Miles, R. Ringuette, T. J. Roth, E. Silich, R. Wearmouth, C. Whitaker, K. W. White
Department of Physics and Astronomy, University of Iowa
Van Allen Hall, Iowa City, IA 52242, USA
philip-kaaret@uiowa.edu

K. Jahoda, T.E. Johnson, M. Matthews, L.H. Santos, B. Dingwall
NASA Goddard Space Flight Center
Greenbelt, MD 20771, USA

S. Schneider, C. Esser, T. Golden, D. Laczkowski
Blue Canyon Technologies
5330 Airport Blvd, Boulder, CO 80301, USA

K.D. Kuntz
The Henry A. Rowland Department of Physics and Astronomy, Johns Hopkins University
3701 San Martin Drive, Baltimore, MD 21218, USA

D. Koutroumpa
Université Versailles Saint-Quentin, LATMOS
11 Boulevard d'Alembert, 78280 Guyancourt, France

ABSTRACT

HaloSat is the first CubeSat for astrophysics funded by NASA's Science Mission Directorate and is designed to map soft X-ray oxygen line emission across the sky in order to constrain the mass and spatial distribution of hot gas in the Milky Way. HaloSat will help determine if hot halos with temperatures near a million degrees bound to galaxies make a significant contribution to the cosmological budget of the normal matter (baryons). HaloSat was deployed from the International Space Station in July 2018 and began routine science operations in October 2018. We describe the on-orbit performance including calibration of the X-ray detectors and initial scientific results including an observation of a halo field and an observation of solar wind charge exchange emission from the helium-focusing cone.

INTRODUCTION

HaloSat is a 6U CubeSat that is currently performing an all-sky survey of line emission from highly ionized oxygen with the goal of measuring the baryonic mass of the Milky Way's halo. As of this writing, the HaloSat spacecraft and science instrument are operating well and the primary mission of mapping soft X-ray line emission from highly ionized oxygen is underway.

HaloSat consists of a science instrument that is a wide-field, soft X-ray spectrometer and a spacecraft bus that provides power, attitude control, communications, and control and data handling. The design, construction, and environmental testing of HaloSat were described previously.[1] Here, we provide brief summaries of the mission goals and science instrument design and then describe the on-orbit performance of the instrument and the first science results.

MISSION GOALS

Baryons are particles with three quarks. The only stable baryons are protons and also neutrons bound within atomic nuclei. The cosmic microwave background shows the universe when it was 400,000 years old and reveals that the universe was homogeneous with a temperature near 3000 K and that baryons constituted 4.87%±0.18% of the total mass/energy present.[2] In the present-day universe, baryons are present at many different temperatures, complicating the task of identifying them all. The best available census reveals only two thirds of the baryons seen in the early Universe.[3] The missing baryons are thought to be gas at

millions of degrees Kelvin. They may be in halos gravitationally bound to individual galaxies, in filaments stretching between galaxies, or some combination.[4,5]

The primary science goal of HaloSat is to estimate the mass of the hot halo surrounding our Milky Way galaxy. At temperatures near 10^6 K, the most cosmically abundant elements, hydrogen and helium, are completely ionized. HaloSat is designed to measure line emission from oxygen, the third most abundant element. Oxygen at 10^6 K is highly ionized with only one or two electrons remaining bound and produces strong emission lines near 574 eV (a triplet of lines from six times ionized oxygen denoted O VII) and 654 eV (a doublet from O VIII) in the soft X-ray range. The Milky Way's halo fills the entire sky, thus very modest angular resolution of 15° or less is required to map the emission. HaloSat will survey at least 75% of the sky with a goal of surveying the entire sky.

The figure of merit for observing diffuse emission is a telescope's field of view times its effective area, or 'grasp'. HaloSat uses three small detectors. Each has an effective area for X-rays of 600 eV of about 8 mm^2, roughly the size of the pupil of a human eye. However, HaloSat's field of view is near 100 square degrees, enabling it to efficiently survey the sky. The grasp of HaloSat is 26 cm^2 deg^2. This is about 20× the grasp of the Chandra X-ray Observatory, NASA Great Observatory for the X-ray band, and about 1/12th the grasp of ESA's X-Ray Multimirror Mission XMM-Newton. Thus, for survey efficiency, a CubeSat can be competitive with a major space observatory.

The accuracy of current emission line measurements of the halo is limited by foreground oxygen emission produced by solar-wind charge exchange (SWCX), when energetic particles in the solar wind exchange charge with neutral atoms within the solar system. HaloSat observes towards the anti-Sun direction during the nighttime half of its 93-minute orbit around Earth to minimize this foreground. This is not possible with XMM-Newton because it has a fixed solar array that restricts observations to a Sun angle range of 70°-110°. Also, HaloSat has a secondary science goal to improve our understanding of SWCX emission and conducts observations specifically devoted to this goal.

SCIENCE INSTRUMENT

The HaloSat science instrument consists of three identical detector units each containing an X-ray detector assembly and signal processing electronics.[1] Each detector unit is independent of the others to eliminate susceptibility to single point failures.

Silicon drift detectors (SDDs) from Amptek, Inc., are used by HaloSat to detect X-rays. The X-ray sensitive element along with a multilayer collimator and a thermoelectric cooler is encapsulated in a TO-8 package enclosed by an entrance window made of Si_3N_4 covered with a thin layer of aluminum. Energy-dependent window transmission is modelled based on the known composition and material thicknesses. The transmission is about 34% at 600 eV and drops to 4% at 300 eV, limiting the lower energy band pass of the instrument. The SDD has an active area of 17 mm^2 and is cooled to -30 C and biased to -135 V during operation. The SDD provides no imaging capability.

To minimize background from charged particle interactions and the diffuse X-ray background, each SDD is surrounded by a shield made of 1.2 mm thick copper-tungsten metal matrix composite electroplated with a 2.5 μm layer of nickel and an outer 1.3 μm layer of gold. The shield has a circular aperture through which the SDD views the sky.
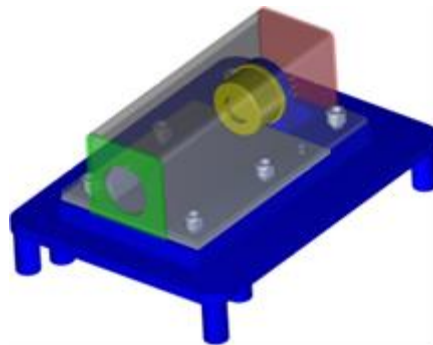
Figure 1: Schematic of an X-ray detector assembly with the SDD in gold.[1] The copper-tungsten passive shield is shown in semi-transparent grey with red and green ends and a solid grey bottom panel. The assembly is mounted on a 'baseplate' shown in blue. The frontend electronics are mounted on the underside of the baseplate in order to minimize the path length for signal from the SDD.

Each detector is mounted in a compartment inside the instrument chassis made of aluminum. The detector is mounted towards the back and there is a 0.78 mm thick aluminum washer at the front with a circular aperture that defines the field of view (FoV). The full-response radius was measured in ground testing to be 5.02° and the zero-response radius to be 7.03° with a linear decrease between. The response-weighted effective field of view is then 0.0350 steradians. A flat mirror on the front of the instrument chassis was used to measure the alignment between the instrument and the spacecraft.

The charge pulse from each X-ray accumulates at the SDD anode and is converted to a voltage signal by a preamplifier with its input field-effect transistor mounted near the SDD and cooled. The signal is processed through a preamplifier and a shaping amplifier, both on a printed circuit board (PCB) near the detector, followed by lower and upper level discriminators, a peak hold circuit (Amptek PH300), and an analog to digital converter. The latter are mounted on a PCB that closes off the detector compartment in the chassis and also contains circuits for power conditioning and serial communications with the bus. Pulses triggering the lower level discriminator are digitized and the pulse height and time of arrival, accurate to 0.05 s, are recorded. Data handling is accomplished with a data-processing unit (DPU) which is a Microsemi A3PE1500 field-programmable gate array programmed with a Z180 microprocessor core on a separate PCB. We refer to the detector units using numbers encoded into their DPUs which are 14, 54, and 38 as viewed from left to right in Figure 2.
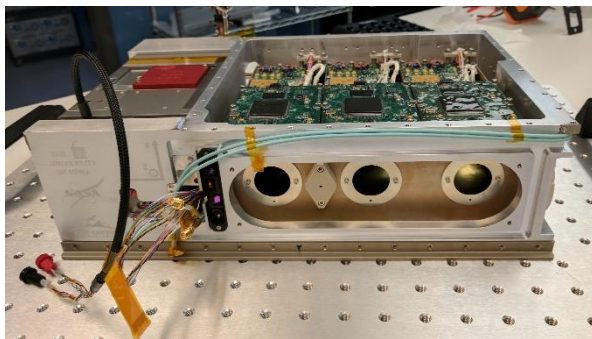
Figure 2: Science instrument integrated with the avionics in the flight bus chassis. PCBs for analog electronics and DPUs are on the top of instrument chassis with the alignment washers and a cover over the optical alignment mirror at the front. The XB1 bus is on the left. The solar array had not been attached at this point in the integration.

The X-ray energy to pulse height conversion was measured during ground calibration with the detectors illuminated either by an X-ray beam with fluorescence emission at the F Kα line (676.8 eV) from a Teflon target along with lines from Al, Si, Cr, and Fe, or by a 55Fe radioactive source.[1] Measurements were made at instrument temperatures ranging from -25°C and +40°C. The energy resolution was measured to be 88.3±3.5, 84.3±2.8, and 82.0±1.4 eV at the F Kα line and 138.5±2.1, 136.5±0.8, and 137.3±1.9 eV at the Mn Kα line for DPUs 14, 54, and 38, respectively. Response matrices were prepared using the ground calibration data using software that models the response of silicon detectors.[6] The software was modified for the SDDs used

for NASA's Neutron star Interior Composition Explorer (NICER) instrument and kindly provided to us by Dr. Jack Steiner of MIT. The NICER SDDs are identical to those on HaloSat except for use of a thinner window, so we tuned the parameters relevant for the HaloSat SDD windows and created effective area versus energy files based on window data supplied by Amptek, Inc., and HS-Foils, Oy.[7] Our response files are compatible with the Xspec spectral fitting software which is commonly used in X-ray astronomy.[8]

SPACECRAFT BUS AND OPERATIONS

The spacecraft bus was built by Blue Canyon Technologies, Inc. (BCT) and has a 6U format with with roughly 4U of the volume allocated for the science payload, 1.5U of the volume allocated for the spacecraft avionics, and 0.5U of the volume allocated for the payload-to-spacecraft interface. Power is provided by the deployable solar panels. The bus has an attitude control systems with star trackers, reaction wheels, and torque rods that can be slewed at 2°/sec and point at inertial targets with an accuracy of ±0.002° (1-σ).[9] An onboard CADET radio is used to downlink telemetry to and receive commands from a ground station at NASA Wallops Flight Facility. A GlobalStar radio provides occasional housekeeping information. Figure 2 shows the spacecraft bus with the science payload integrated with the instrument cover removed and Figure 3 shows several happy team members during science instrument integration.

Figure 3: Members of the HaloSat team during integration at BCT. HaloSat is visible near the center.

Funding for HaloSat began in January 2016 and the science instrument was integrated with the spacecraft in October 2017. Halosat was integrated into a Nanoracks deployer in March 2018, was launched in May 2018 on the Orbital ATK OA-9 mission, was deployed from the International Space Station in July 2018, see Figure 4, and began science operations in October 2018. The longer than expected commissioning phase was largely due to communications issues, subsequently resolved with achievement of our design downlink speed of 3 Mbps, and issues with the simultaneous commissioning of the three CubeSats with nearly identical orbits using a

single ground station. BCT runs mission operations including command preparation and uplink, telemetry downlink, spacecraft bus state of health monitoring, and fault recovery. The University of Iowa prepares the science observing program, monitors the instrument state of health, and processes all science data. Science observations are carried out during the night-side half of each spacecraft orbit with two targets observed for about 1300 seconds each.

Figure 4: Deployment of HaloSat (on the right) with RainCube (on the left) from the ISS.

**ON-ORBIT PERFORMANCE**

Pointing and Field of View

The Crab is a pulsar wind nebula powered by a young pulsar with a spin period of about 33 milliseconds. The Crab has been used as a calibration target since the early days of X-ray astronomy.[10] We used the Crab to measure the alignment between the boresights of the X-ray instruments and the coordinate system defined by the star trackers on the spacecraft bus.

We performed a series of slew maneuvers in which the science instrument was pointed towards the Crab and then the pointing was gradually offset while the spacecraft roll angle was held fixed. Eight different maneuvers were performed corresponding to eight different roll angles at equal intervals in the spacecraft frame. The X-ray count rate versus offset data were fitted to a model matching the FoV measured on the ground with the FoV center being a fitted parameter. The count rate for DPU 54 versus radial offset from the fitted center for the best fitted model are shown in Figure 5. We found an offset of about 1.0° in the spacecraft Y direction from the nominal pre-flight instrument boresight. This correction was applied to the pointing of observations obtained after 1 December 2018. After the correction, another pointing test was performed and the

fitted FoV center is consistent with the expected position within ±0.09° in the spacecraft X direction and ±0.18° in the spacecraft Y direction for all DPUs. We conclude that the pointing of the X-ray boresight of HaloSat is accurate to ±0.2°, which is a small fraction of the FoV. The X-ray pointing uncertainty is dominated by the accuracy to which we are able to measure the relative alignment between the X-ray detectors and the spacecraft reference frame. The median offset between the commanded target position during observations and the spacecraft pointing measured by the attitude control system is 0.0007°, see Figure 6.
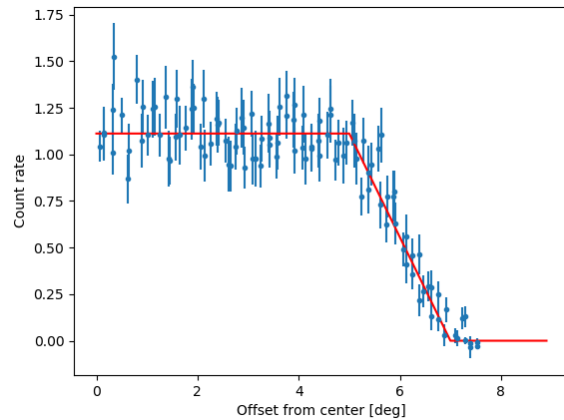
Figure 5: X-ray count rate versus pointing offset from the Crab for DPU 54.
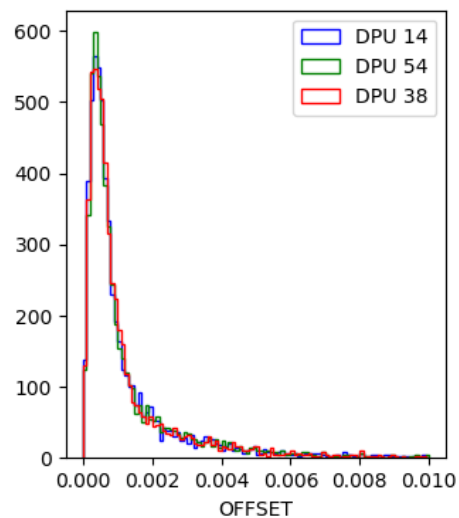
Figure 6: Histogram of pointing offsets in 8-second intervals.
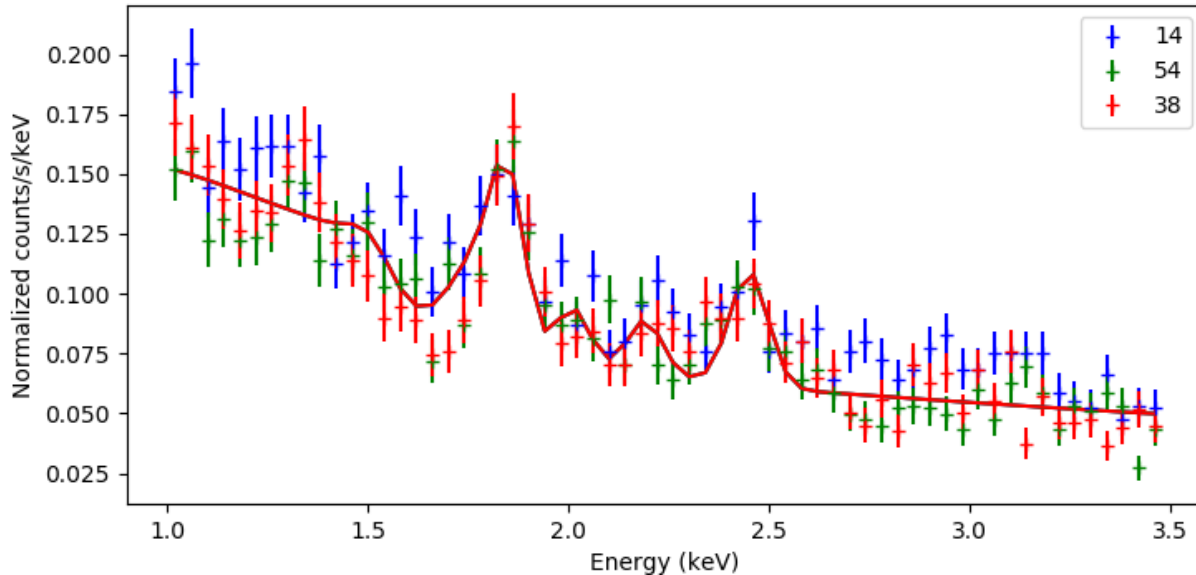
Figure 7: X-ray spectra of the Cas A field. Data from all three detectors are shown as indicated by the DPU number in the legend, 14=black, 54=red, 38=green. Prominent emission lines are visible from Si XIII at 1.86 keV and 2.18 keV, S XV at 2.45 keV, and S XIV at 2.01 keV. These spectra use the ground energy scale calibration with no temperature correction applied.

Spectral Response

To check the on-orbit X-ray energy scale calibration, we examined spectra obtained while observing the dark side of the Earth, Cassiopeia A, and the Vela supernova. The dark Earth observations show an aluminum line likely due to fluorescence by energetic particles. The fitted centroids of that line are consistent with no shift in the energy response relative to the ground calibration with statistical accuracies of 0.4% to 1.4% for the different DPUs.

Cas A is a young supernova remnant (SNR) with an age of about 300 years and has strong emission lines from heavy elements in its X-ray spectrum. X-ray emission lines from Mg, Si, S, and Ar were first detected with the solid-state spectrometer on Einstein and first mapped with ASCA.[11,12] Cas A has been used to calibrate the energy scale of several X-ray instruments.[13]

The HaloSat field centered on Cas A includes another SNR, CTB 109, and several point sources, but the emission is dominated by Cas A. We extracted spectra of the Cas A for all three DPUs, see Figure 7, and fitted them in the 1.0-3.5 keV range with a model consisting of a powerlaw and four Gaussians with line energies fixed to 1.8558 keV (Si XIII), 2.4515 keV (S XV), 2.0053 keV (S XIV), and 2.1830 keV (Si XIII). Line energies were extracted from the AtomDB database of atomic transitions and centroids for blends were calculated from

their relative intensities (http://atomdb.org). The continuum X-ray spectrum of Cas A is typically described as the sum of two thermal plasma components and a powerlaw, but a single powerlaw produces an adequate fit over the limited energy band used in the fit. The line widths are consistent with the energy resolution measured during the ground calibration. Allowing the slope of the channel to energy conversion to vary reduced the χ^2/DoF of the fit from 611.9/366 to 589.8/363 and resulted in gain slope correction factors of $1.0022_{-0.0033}^{+0.0009}$, 1.0027 ± 0.0007, and 1.0031 ± 0.0008 for DPU 14, 54, and 38 respectively. This may suggest a small change, 0.3% or less, in the ADC channel to energy conversion from the ground calibration to flight.

The Vela SNR is one of the brightest soft X-ray sources and has a diameter of 8°.[14] We extracted spectra in the 0.5-3.0 keV band for each DPU for a field centered on Vela and including the Puppis A SNR, see Figure 8. The spectra were fitted with a model consisting of absorbed cool and hot thermal plasma components modeled using the apec and vapec models in Xspec, respectively, and an absorbed broken powerlaw for the cosmic X-ray background (CXB), and a powerlaw for the instrumental background. Allowing the slope of the channel to energy conversion to vary reduced the χ^2/DoF of the fit from 610.9/362 to 583.0/359 and the gain slope correction factors were, again, 0.3% or less with 0.9999 ± 0.0001, 1.0020 ± 0.0003, and 1.0030 ± 0.0002 for DPU 14, 54, and 38 respectively.
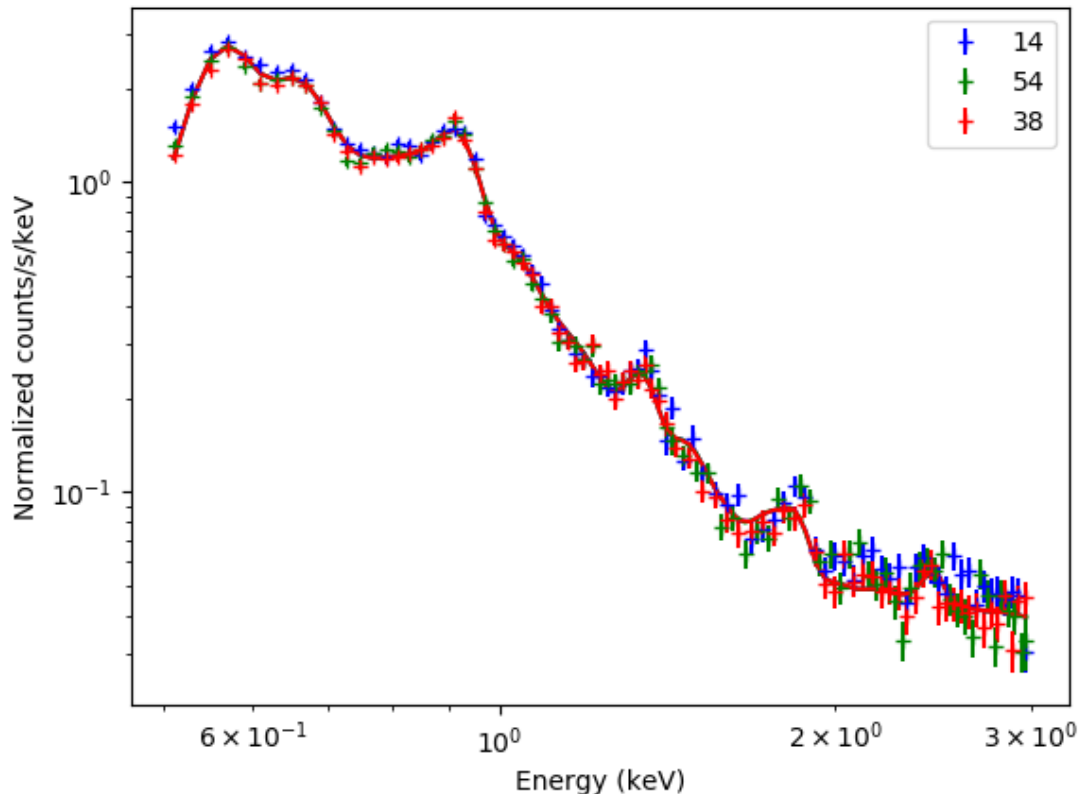
Figure 8: X-ray spectra of the Vela SNR field.

We chose to use the temperature-averaged ground calibration for the analysis presented below.

Effective Area

We also use the Crab to calibrate the effective area of HaloSat. The Crab is often used as a 'standard candle' in X-ray astronomy.[10,13,15] However, it does exhibit variability of up to 7% in the 10-100 keV band on long time scales.[16]

We extracted Crab spectra for each detector unit and applied the flight energy calibration described in the previous section. Due to HaloSat's large FoV, the spectra also contain diffuse emission, so we extracted a background spectrum from a nearby region centered at $(\alpha, \delta) = (82.64°, 34.01°)$ (J2000) with a similar level of diffuse emission and no bright X-ray point sources. The Crab spectrum is well modeled as a simple absorbed powerlaw. We used the response matrices and gain corrections discussed previously and the tbabs model in Xspec to describe the interstellar absorption.[17]

The science of HaloSat is focused on line emission in the 0.5-2.0 keV band. The Crab flux in that band depends on all of the model parameters, so we prefer to directly compare observed fluxes rather than model parameters. Most of the previously published results on Milky Way halo emission use XMM-Newton which has two imaging instruments, the EPIC-MOS and the EPIC-pn. Unfortunately, the MOS suffers from pileup during observations of the Crab and the only Crab normalizations reported for XMM are for the EPIC-pn. We adopt measurements of the Crab spectrum with the EPIC-pn, in particular the model calculated by Kirch and coauthors using Wilms abundances and Verner cross-sections, giving a flux of 9.35×10^{-9} erg cm^{-2} s^{-1}, to calibrate the effective area of HaloSat.[18] This flux is within 4% of the Crab flux of model 3* of Weisskopf and coauthors for the EPIC-pn.[19]

We apply a correction factor to the auxiliary response files described above to bring the HaloSat fluxes into agreement with the Crab flux given by Kirch and collaborators. We chose not to adjust any other response matrix parameters using the Crab spectrum as the strong interstellar absorption makes such tuning problematic for our energy band of interest. The fluxes for all three DPUs are consistent within the measurement error of 2.5%, so a single correction factor is used.
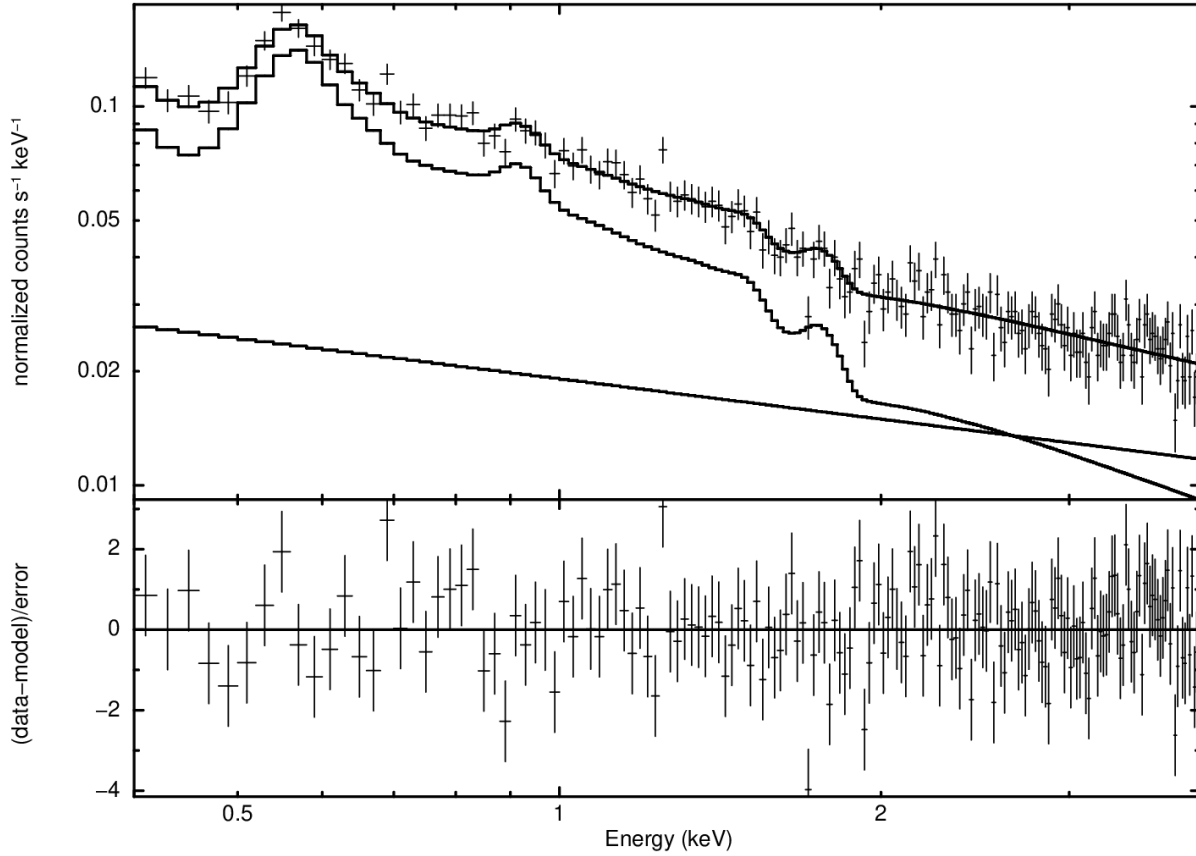
Figure 9: Spectrum of a halo field at (l = 166°, b = 62°) observed for 40 ks of good time with counts from all three detectors summed. The lowest line at 1 keV is the instrumental background, the middle curve is the astrophysical spectrum, the top curve is the sum.

INITIAL HALO SCIENCE RESULTS

The scientific goal of HaloSat is to constrain the mass and spatial distribution of hot gas associated with the Milky Way by mapping the emission in the O VII and O VIII lines. The observational goal is to reach a statistical accuracy of ±0.5 LU on the sum of the O VII and O VIII line emission for fields with a line strength near 5 LU (where LU = line unit = photon cm^{-2} s^{-1} $ster^{-1}$).

Figure 9 shows a spectrum obtained for a high Galactic latitude field at (l= 166°, b= 62°) from an observation with an exposure of 40 ks after background and data quality screening. The gain and effective area corrections described above were applied and the counts from all three detectors were summed.

We fitted the data with a model consisting of Gaussians at 568.4 and 653.7 eV for the O VII and O VIII line emission and an absorbed thermal plasma with oxygen line emission removed.[20] We added an absorbed double broken powerlaw for the CXB.[21] The first broken powerlaw has a break energy of 1.2 keV, a photon index below the break of 1.54, a photon index above the break

of 1.4, and a normalization at 1 keV fixed to 5.7 photon cm^{-2} s^{-1} keV^{-1} $ster^{-1}$. The second broken powerlaw has the same parameters except the photon index below the break is 1.96 and the normalization is free. We also added a powerlaw not modified by the response matrix for particle background.

We obtained a good fit with $\chi^2/DoF = 188.8/172$. The free CXB normalization is 5.1±2.3 photon cm^{-2} s^{-1} kev^{-1} $ster^{-1}$ and the total CXB flux is in good agreement with previously measured values, which provides a confirmation of our flux normalization.[22] The O VII flux is 3.26±0.41 LU. The statistical accuracy meets our observational goal.

In order to measure the properties of the halo, we must conduct similar observations over a large fraction of the sky, analyze the data, and then fit our measurements of the oxygen line intensities to models of the halo to infer its properties. Our goal is to survey the entire sky, although only fields above and below the Galactic plane will be useful in constraining the properties of the halo.
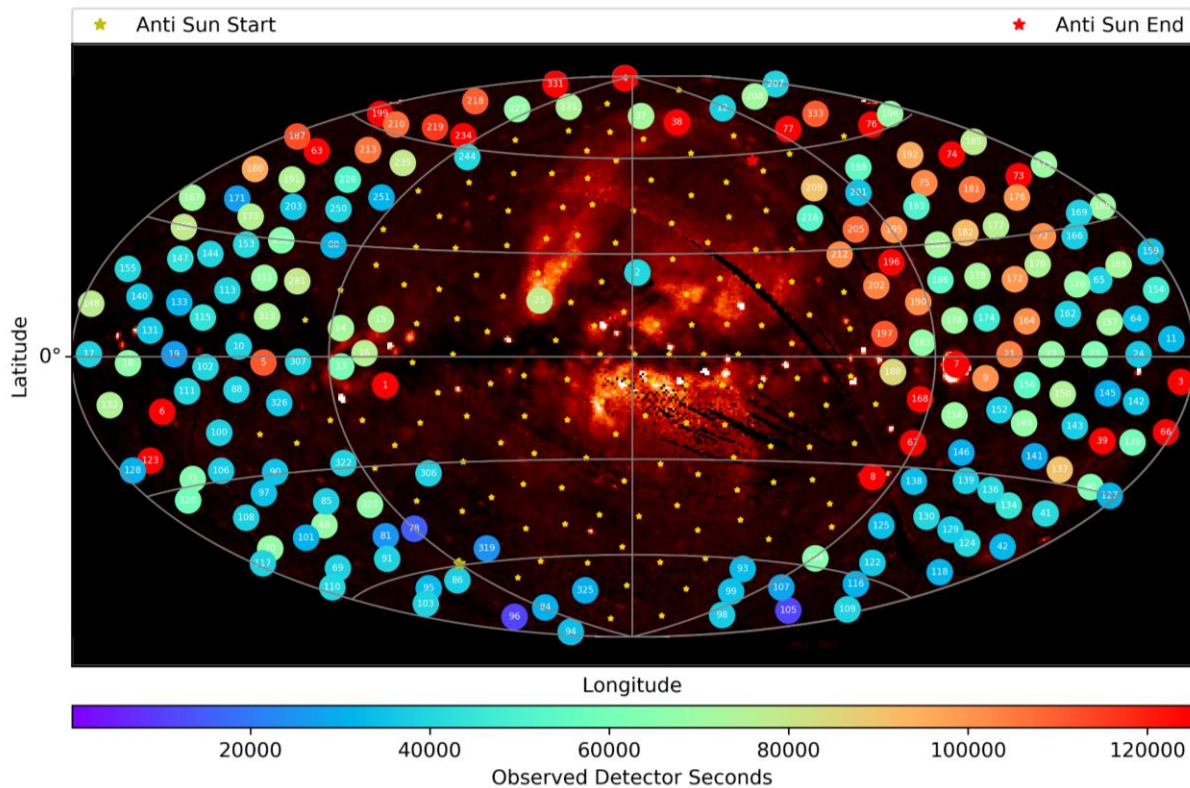
Figure 10: Observations obtained to date with HaloSat. Fields already observed are shown as circles (smaller than the field of view) with color indicating the total exposure obtained. Stars mark fields that have not yet been observed. The plot is in Galactic coordinates with the center of the Milky Way at the center and Galactic North towards the top. The image is a map of diffuse soft X-ray emission from the ROSAT observatory.[23]

We have selected 333 observation fields that tile the sky given HaloSat's field of view, see Figure 10.

As of this writing, we have surveyed approximately one third of the sky with deep coverage and one third with shallower coverage. We should be able to survey the entire sky with the operations currently planned and funded until October 2019. We have applied for funding for a mission extension to June 2020 that would enable us to perform deeper observations, including a second measurement of the helium focusing cone as described in the next section.
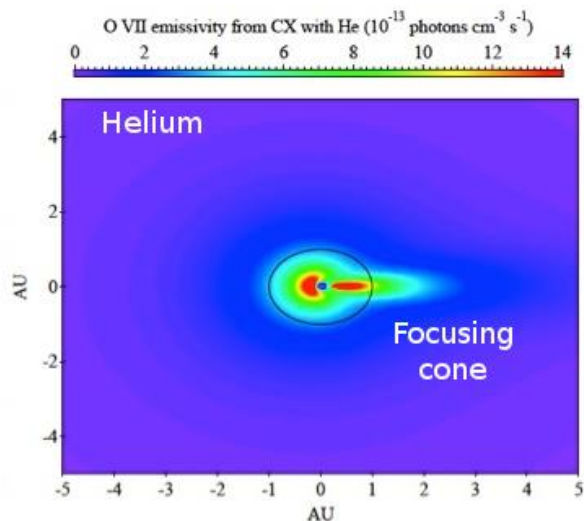
SOLAR WIND CHARGE EXCHANGE

Solar wind charge exchange (SWCX) emission occurs when a highly charged ion of the solar wind picks up an electron from a neutral atom forming an excited ion that decays by emitting an X-ray.[24] SWCX emission is produced within Earth's magnetosheath and throughout the heliosphere. In the magnetosphere, the neutral targets are H atoms in the Earth's exosphere. In the heliosphere, the targets are interstellar H and He atoms flowing through interplanetary space. The SWCX line flux is the integral over the line of sight of the product of the ion density, the neutral density, the relative velocity between the two, the charge exchange cross-section, and the individual line emission probability. The magnetosheath responds rapidly to changes in the solar wind flux, so its SWCX emission is strongly time-variable and dependent on observation geometry. The heliospheric emission is integrated over a long line of sight, effectively over a month of solar wind conditions, and varies more slowly.

SWCX emission is currently the dominant uncertainty in the oxygen line intensity measurement of the halo.[25] Our observing strategy, discussed above, should minimize SWCX contamination. We are also making observations specifically to study SWCX that should improve the accuracy with which we can model the remaining SWCX emission and, thus, improve the accuracy of our measurements of the Milky Way's halo.

The distribution of heliospheric emission is determined by the geometry of the target gas. Neutral interstellar gas flows at ~25 km/s through the Solar System, see Figure 11. This gas, mostly hydrogen but with ~15% helium, flows from the Galactic direction (l ~ 3°, b ~ 16°), placing the Earth downstream of the Sun in early December. The flow of interstellar hydrogen is affected by both radiation pressure and gravity, and the hydrogen becomes strongly ionized through charge exchange with solar protons and photo-ionization so that the hydrogen is denser upstream than downstream. In contrast, the interstellar helium flow is not strongly ionized but is affected mainly by gravity, which focuses the flow downstream of the Sun into the "He-focusing cone." As seen from the Sun, the heliospheric SWCX emission appears roughly axisymmetric around the interstellar wind axis, save for latitudinal variations due to the anisotropy of the solar wind flux. For satellites in low Earth orbit, the change in vantage point as the Earth orbits the Sun induces parallax effects to the heliospheric intensity.

Figure 11: He-focusing cone. The figure shows emissivity within the ecliptic plane of heliospheric O VII solar wind charge exchange (SWCX). The Sun is at the center of the figure and distances are marked in astronomical units (AU) equal to the Sun-Earth distance. The ellipse shows Earth's orbit.

The heliospheric OVII and OVIII emission are calculated from the interstellar neutral H and He distributions and measurements of the solar wind provided by solar and heliospheric observatories.[26] A crucial input to this modeling is knowledge of the O-He interaction cross section.[27] HaloSat can perform such a measurement by observing along the H-focusing cone as the Earth passes through and then correlating the observed soft X-ray emission with the He distribution

along the line of sight. We performed a series of such measurements when HaloSat (and the Earth) passed through the He-focusing cone in December 2018 with observations made at monthly intervals from two months before the passage to two months after. Our preliminary spectrum from one month before passage is shown in Figure 12.

The spectrum was fitted with a model of the heliospheric emission which has only the normalization as a free parameter. The model also included a broken powerlaw for the CXB and a powerlaw for the instrumental background. The SWCX emission model fits very well except that the Mg XI line at 1.35 keV is stronger in the model than the data. This likely indicates that the Mg ions charge-exchanging to produce this line were less abundant in the solar wind than the standard values in the reference spectrum. The HaloSat spectrum shows that HaloSat can accurately measure SWCX emission. These observations cannot be done by any other current observatory. These HaloSat measurements will provide an accurate measurement of the O-He cross section and an absolute scale for the SWCX models.

CONCLUSIONS

HaloSat has demonstrated that CubeSats can be the effective vehicles for astrophysics research. The commercialization of small satellite technologies enabled construction of HaloSat at a modest cost of $3.7M. This required accepting already engineered solutions with few or no modifications and adapting the instrument design to existing capabilities and interfaces of the commercial bus and components but resulted in a cost far below what would have been required to develop all of the components from scratch and also lower risk due to the heritage of the subsystems. The success of HaloSat should encourage construction of more CubeSats for astrophysics using a commercial bus that enables the science team to focus their efforts in instrument development where their expertise lies.

One of NASA's key astrophysics science objectives is to understand the origin and destiny of the universe. HaloSat should enable a significant advance in our understanding of the geometry of the hot halo of the Milky Way by distinguishing between extended and compact halo models and constraining the baryonic mass of the Milky Way.

NASA's key heliophysics science goal is to understand the Sun and its interactions with the Earth and the solar system. HaloSat will provide a unique data set for the study of the interaction of the solar wind with the heliosphere and the magnetosphere via solar wind charge exchange emission and enable a new measurement of the O-He interaction cross-section.
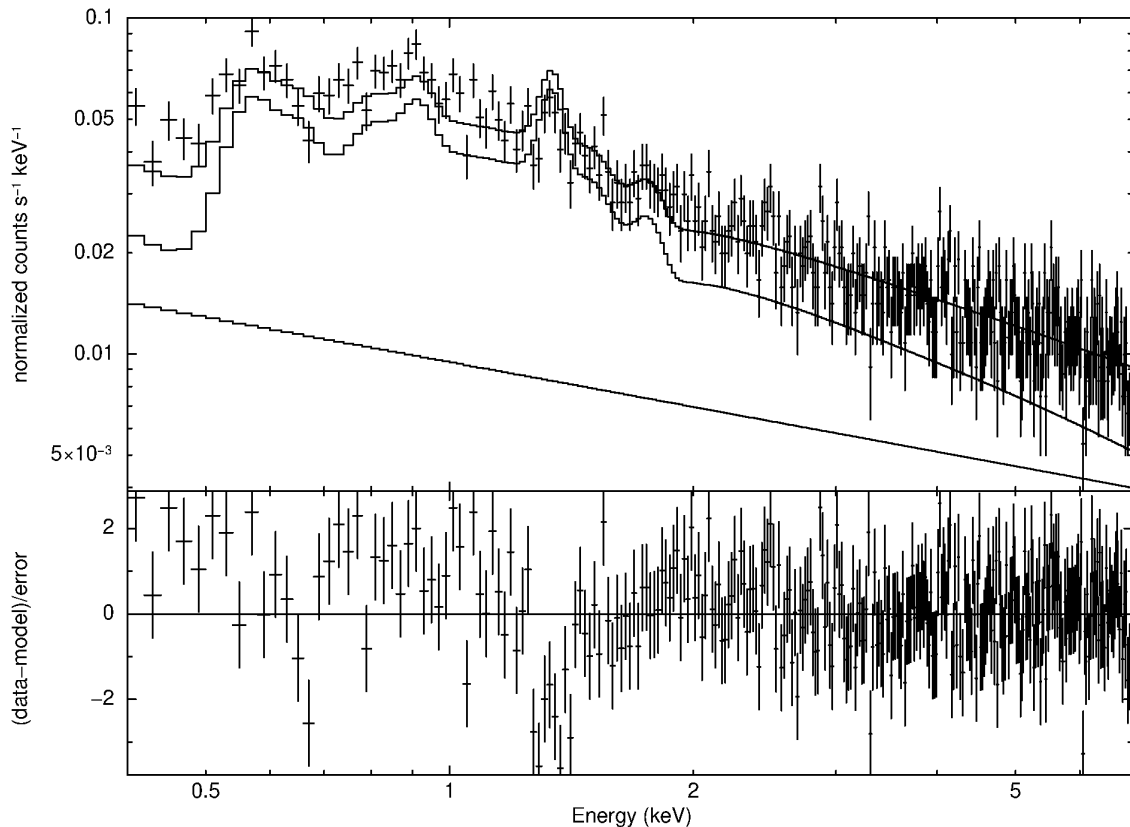
Figure 12: HaloSat X-ray spectrum of solar wind charge exchange emission in the He-focusing cone taken one month before the Earth passed through the cone. The residuals indicate an underabundance of Mg XI ions.

The HaloSat program has helped train the next generation of scientists and engineers who will execute NASA's future missions. Three graduate students, two of whom are writing theses on HaloSat, and nine undergraduates in physics, astronomy, and engineering, several of whom have won Iowa Space Grant Scholarship and one of whom was named the University of Iowa's second most influential undergraduate in 2019 by College Magazine, have worked on HaloSat. HaloSat has trained two postdoctoral research scientists, one of whom has moved to a research scientist position at NASA/GSFC.

References

1. Zajczyk, A., Kaaret, P., Kirchner, D.L., LaRocca, D., Robison, W.T., Fuelberth, W., Gulick, H.C., Haworth, J., McCurdy, R., Miles, D., Wearmouth, R., White, K., Jahoda, K., Johnson, T.E., Matthews, M., Santos, L.H., Snowden, S.L., Kuntz, K.D., Schneider, S., Esser, C., Golden, T., Hansen, K., Hanslik, K., & Koutroumpa, D., "HaloSat: a search for missing baryons with a CubeSat", 32nd Annual AIAA/USU Conference on Small Satellites, SSC18-WKIX-01, 2018.

2. Planck Collaboration, "Planck 2013 results. XVI. Cosmological parameters", Astronomy & Astrophysics, 571, A16, 2014.

3. Shull, J.M., Smith, B.D., and Danforth, C.W., "The Baryon Census in a Multiphase Intergalactic Medium: 30% of the Baryons May Still be Missing", Astrophysical Journal, 759, 23, 2012.

4. Gupta, A., Mathur, S., Krongold, Y., Nicastro, F., and Galeazzi, M., "A Huge Reservoir of Ionized Gas around the Milky Way: Accounting for the Missing Mass?", Astrophysical Journal, 756, L8, 2012.

5. Cen, R. and Ostriker, J.P., ``Where Are the Baryons?'', Astrophysical Journal 514, 1-6, 1999.

6. Scholze, F. and Procop, M., "Modelling the response function of energy dispersive X-ray spectrometers with silicon detectors", X-Ray Spectrometry, 38, 312–321, 2009.

7. Gendreau, K.C., Arzoumanian, Z. et al., "The Neutron star Interior Composition ExploreR (NICER): Design and Development", Proceedings of SPIE 9905, 99051H, 2016.

8. Arnaud, K.A., 1996, Astronomical Data Analysis Software and Systems V, eds. Jacoby G. and Barnes J., p17, ASP Conf. Series volume 101.

9. Hegel, D., "FlexCore: Low-Cost Attitude Determination and Control Enabling High-Performance Small Spacecraft", 30th Annual AIAA/USU Conference on Small Satellites, SSC16-X-7, 2016.

10. Toor, A. and Seward, F. D., "The Crab Nebula as a calibration source for X-ray astronomy", Astronomical Journal 79, 995-999, 1974.

11. Becker, R.H., Holt, S.S., Smith, B.W., White, N.E., Boldt, E.A., Mushotzky, R.F., and Serlemitsos, P.J., "X-ray spectrum of Cassiopeia A measured with the Einstein SSS", Astrophysical Journal 234, L73, 1979.

12. Holt, S.S., Gotthelf, E.V., Tsunemi, H., Negoro, H. 1994, "ASCA observations of Cassiopeia A", Publications of the Astronomical Society of Japan, 46, L151.

13. Jahoda, K., Markwardt, C.B., Radeva, Y., Rots, A.H., Stark, M.J., Swank, J.H., Strohmayer, T.E., and Zhang, W., "Calibration of the Rossi X-ray timing explorer proportional counter array", Astrophysical Journal Supplement Series, 163, 401, 2006.

14. Aschenbach, B., Egger, R., and Trümper, J., "Discovery of Explosion Fragments Outside the Vela Supernova Remnant Shock-Wave Boundary", Nature, 373, 587, 1995.

15. Madsen, K.K., Harrison, F.A., Markwardt, C.B., An, H., Grefenstette, B.W., Bachetti, M., Miyasaka, H., Kitaguchi, T., Bhalerao, V., Boggs, S., and Christensen, F.E. 2015, "Calibration of the NuSTAR high-energy focusing X-ray telescope", Astrophysical Journal Supplement Series, 220, 8.

16. Wilson-Hodge, C.A., Cherry, M.L., Case, G.L., Baumgartner, W.H., Beklen, E., Bhat, N.P., Briggs, M.S., Camero-Arranz, A., Chaplin, V., Connaughton, V., Finger, M.H., Gehrels, N., Greiner, J., Jahoda, K., Jenke, P., Kippen, R.M., Kouveliotou, C., Krimm, H.A., Kuulkers, E., Lund, N., Meegan, C.A., Natalucci, L., Paciesas, W.S., Preece, R., Rodi, J.C., Shaposhnikov, N., Skinner, G.K., Swartz, D. von Kienlin, A., Diehl, R., and Zhang, X.-L., "When a Standard Candle Flickers", Astrophys. J. Lett. 727, L40, 2011.

17. Wilms, J., Allen, A., and McCray, R., "On the absorption of X-rays in the interstellar medium", Astrophysical Journal 542(2), 914, 2000.

18. Kirsch, M.G., Briel, U.G., Burrows, D., Campana, S., Cusumano, G., Ebisawa, K., Freyberg, M.J., Guainazzi, M., Haberl, F., Jahoda, K., and Kaastra, J., "Crab: the standard X-ray candle with all (modern) X-ray satellites", Proceedings of SPIE, 5898, 22-33, 2005.

19. Weisskopf, M.C., Guainazzi, M., Jahoda, K., Shaposhnikov, N., O'Dell, S.L., Zavlin, V.E., Wilson-Hodge, C. and Elsner, R.F., "On Calibrations Using the Crab Nebula and Models of the Nebular X-Ray Emission", Astrophysical Journal 713, 912-919, 2010.

20. Henley, D.B., Shelton, R.L., "An XMM-Newton Survey of the Soft X-Ray Background. II. An All-Sky Catalog of Diffuse O VII and O VIII Emission Intensities", Astrophysical Journal Supplement 202, 14, 2012.

21. Smith, R.K., Bautz, M. W., Edgar, R.J., Fujimoto, R., Hamaguchi, K., Hughes, J.P., Ishida, M., Kelley, R., Kilbourne, C. A., Kuntz, K.D.,

McCammon, D., Miller, E., Mitsuda, K., Mukai, K., Plucinsky, P. P., Porter, F. S., Snowden, S. L., Takei, Y., Terada, Y., Tsuboi, Y., Yamasaki, N.Y., "Suzaku Observations of the Local and Distant Hot ISM", Proceeding of the Astronomical Society of Japan 59, 141, 2007.

22. Moretti, A., Pagani, C., Cusumano, G., Campana, S., Perri, M., Abbey, A., Ajello, M., Beardmore, A.P., Burrows, D., Chincarini, G., Godet, O., Guidorzi, C., Hill, J.E., Kennea, J., Nousek, J., Osborne, J.P., and Tagliaferri, G., "A new measurement of the cosmic X-ray background", Astro. Astrophys. 493, 501-509, 2009.

23. Snowden, S.L., Egger, R., Freyberg, M. J., McCammon, D., Plucinsky, P. P., Sanders, W. T., Schmitt, J. H. M. M., Trümper, J., Voges, W. 1997, "ROSAT Survey Diffuse X-Ray Background Maps. II", Astrophys. J. 485, 125.

24. Kuntz, K.D., ``Solar wind charge exchange: an astrophysical nuisance", Astronomy and Astrophysics Review 27, 1, 2019.

25. Slavin, J., Wargelin, B.J., and Koutroumpa, D., "Solar Wind Charge Exchange Emission in the Chandra Deep Field North", Astrophysical Journal 779, 13, 2013.

26. Koutroumpa, D., Collier, M.R., Kuntz, K.D., Lallement, R., and Snowden, S. L., "Solar Wind Charge Exchange Emission from the Helium Focusing Cone: Model to Data Comparison", Astrophysical Journal 697, 1214, 2009.

27. Galeazzi, M., Chiao, M., Collier, M.R., Cravens, T., Koutroumpa, D., Kuntz, K.D., Lallement, R., Lepri, S.T., McCammon, D., Morgan, K., Porter, F.S., 2014, "The origin of the local 1/4-keV X-ray flux in both charge exchange and a hot bubble", Nature, 512(7513), p.171.